Nanometer-Thick Carbon Coatings with Covalent

Chemical Functionalization of Metal Oxide

Nanoparticles for Environmental and Biological

Applications

Paige C. Kinsley[†], Curtis M. Green[‡], Jaya Borgatta[§], Catherine E. Kruszynski Earl, Elizabeth D.

Laudadio§, Robert J. Hamers*

Department of Chemistry, University of Wisconsin-Madison, 1101 University Avenue, Madison,

WI 53706, USA

*Corresponding Author: rjhamers@wisc.edu

ABSTRACT

Metal oxide nanoparticles have many useful applications in environmental studies, as tracking

agents in life sciences, and nutrient delivery for nano-enhanced agriculture. A key challenge in

controlling the behavior of metal oxide nanoparticles in aqueous media is that molecular ligands

are unstable with respect to hydrolytic cleavage from the surfaces. This instability limits the

practical application of metal oxide nanoparticles in aqueous media. We have developed a method

for producing a nanometer-thin carbon shells on the surface of Al₂O₃, Cr ³⁺:Al₂O₃ (nano-ruby),

1

ZnO, and Fe $_3$ O $_4$ (magnetite) metal oxides that provides a scaffold for subsequent covalent chemical functionalization. Fluorescence measurements using carbonized Cr $^{3+}$:Al $_2$ O $_3$ (nanoruby) confirm that these thin carbon coatings have relatively impact on the optical properties, allowing bright emission with less than 50% decrease in fluorescence intensity compared to identical nanoruby without carbon coating. We demonstrate the utility for functionalization by modifying C-coated Al $_2$ O $_3$ with molecular ligands bearing positive and negative charges. This approach provides a pathway for functionalization of a broad range of metal oxide nanoparticles with molecular ligands that can confer specific molecular properties to the nanoparticle surfaces in aqueous media while taking advantage of the high strength and stability of C-C interfacial bonds between surface ligands and the carbon shell.

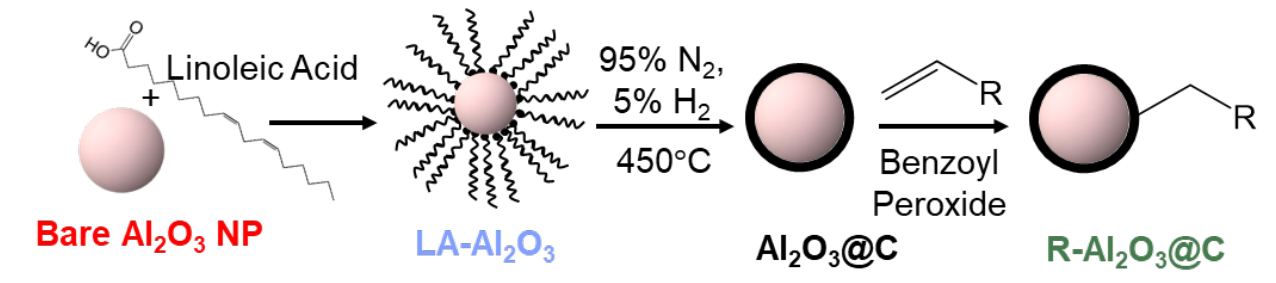
Keywords: Carbon; Functionalization; Surface Chemistry; Nano-ruby; Alumina; Nanoparticles INTRODUCTION

The small size and wide range of optical and magnetic properties make metal oxide nanomaterials particularly attractive candidates for use as analytical probes in chemistry and biology. For example, nanoruby (Al₂O₃:Cr³⁺) has a broad absorption spectrum coupled with a single very sharp emission line and quantum efficiency exceeding 80%; these properties make it well suited to applications based on imaging and tracking in complex biological systems. Iron oxide nanoparticles exhibit useful magnetic properties, facilitating fundamental studies of protein adsorption and potential use in biomedical diagnostics and therapy and diagnostics. Recent studies have shown that metal oxides can also be highly effective micronutrient delivery vehicles for nano-enhanced agriculture. Control over the particle surface could increase their efficiency and effectiveness, targeting specific parts of plants or bodies for delivery of nutrients or drugs.

In many of these applications, the utility of the nanoparticle arises from a bulk material property (e.g., magnetic or optical), but the surface functional groups and their associated properties (e.g., charge, hydrophobicity) can dictate their subsequent interactions. A key challenge to even more widespread use of metal oxide nanoparticles is the inherent hydrolytic instability of the surface bonds involved in commonly used surface functionalization schemes, 15-16 limiting applicability in aqueous media for biological and environmental studies.¹⁷ For example, nearly all metal-oxygencarbon bonds are hydrolytically unstable with respect to M-O-C + $H_2O \rightarrow M$ -OH + C-OH. ¹⁸⁻²⁰ One strategy for overcoming these instabilities is to form surface cross-links such that removal of the molecular layers requires hydrolysis of multiple bonds.²¹ Among widely used methods, silane monolayers and phosphonic acid layers are stabilized by the formation of Si-O-Si and P-O-P crosslinks, respectively.²²⁻²⁵ While effective for many applications, even these layers are ultimately susceptible to chemical degradation, limiting their overall utility in applications that require layers that are stable over longer periods of time, especially in harsh media such as those found in biological and/or environmental systems.²⁵⁻²⁷ Carboxylic acids have been used extensively as modifiers on metal oxides, but are also reported to degrade rapidly under conditions relevant to biological studies.¹⁷ In contrast with metal oxides, carbon-based materials such as diamond, carbon dots, and amorphous carbon films can be functionalized using strategies yielding an "all-carbon" interfacial structure that provides unparalleled stability. 28-31 These prior studies suggest that it might be possible to functionalize a wide range of metal oxides by using ultra-thin carbon coatings as an interfacial layer, followed by use of the photochemical or radical methods demonstrated previously. A key challenge for many applications is to control the carbon layer thickness such that it does not overwhelm or obscure the desired properties of the underlying metal oxide. For

example, in the case of nanoruby, an ideal carbon coating should be sufficiently thin that it does not adversely impact the optical emission from the encapsulated nanoparticle.

We have developed a method that forms a thin, stable carbon layer on the metal oxide nanoparticle surface, providing a platform for further chemical modification using radical initiation of molecules, as shown in Scheme 1.28 Linoleic acid was chosen as the carbon source because the carboxylic head provides a binding site on the molecule such that a monolayer of molecules will initially adsorb to the metal oxide surface.32 Linoleic acid also contains two points of unsaturation in the alkyl tail, providing potential sites for thermal crosslinking between molecules. After forming an adsorbed layer of linoleic acid on the metal oxide surface, the particles are heated in a closed system in a slightly reducing atmosphere (%5 H₂:95% N₂) to produce a thermally stable carbon shell containing sp²-hybridized and sp³-hybridized carbon. The carbon surface formed after thermal treatment provides a platform for covalent attachment of vinyl molecules with various chemical properties. This carbonization treatment of metal oxides offers a



Scheme 1. Method to form stable carbon coating on metal oxide that can be further covalently functionalized using thermal radical initiator benzoyl peroxide.

general method to tune the surface chemistry of metal oxides for long-term surface functionalization. Stable, covalent functionalization of metal oxides will give control over chemical species present on their surface and allow for deeper insights into nano-bio interactions.

MATERIALS AND METHODS

Materials

Aluminum oxide nanoparticles (alpha phase, 27-43 nm diameter) were purchased from Nanostructured and Amorphous Materials Inc. Zinc oxide nanoparticle (10-30 nm diameter) were purchased from US Research Nanomaterials, Inc. Iron (II,III) oxide nanoparticles (11 ± 3 nm diameter, from TEM) were synthesized as previously reported, described in the supporting information.³³ Ruby (Cr³*:Al₂O₃) nanoparticles (27 ± 14 nm diameter, from TEM) were synthesized following previous work;³⁴ specific procedures used in our work are included in the Supporting Information. Planar single-crystal aluminum oxide wafers were purchased from MTI corporation. 1H,1H-undecafluorohexylamine (>97.0%), arachidonic acid (99%), oleic acid, and cis-11-eicosenoic acid were purchased from Fisher Scientific. Cis-11,14-eicosadienoic acid was purchased from Santa Cruz Biotechnology. Forming gas (95% N₂: 5% H₂) was purchased from Airgas. All other chemicals were purchased from Sigma-Aldrich. A stainless-steel Swagelok cell (parts SS-600-6 and SS-600-C) used for thermal carbonization was purchased from Kurt J. Lesker Company. All water used was prepared by reverse osmosis followed by a Barnstead Nanopure system and exhibited a resistivity of 18.2 MΩ•cm.

Nanomaterial Synthesis and Functionalization

A key step in our work is to control the thickness of the carbon layer that forms on the nanoparticles. In the work reported here, the layer thickness was controlled by first forming a monolayer film on the nanoparticles, followed by heating in a closed container to a temperature sufficiently high that the organic layers decompose and leave a thin layer of carbon on the nanoparticle surfaces. Scheme 1 shows a typical reaction progression, shown for the carbonization of Al_2O_3 NP using linoleic acid. To prepare aluminum oxide nanoparticles for carbonization, Al_2O_3 nanoparticles (1.000 g) were added to hexadecane (20 mL). Linoleic acid (20 μ L) was added, and

the mixture was stirred for 24 h at room temperature. The linoleic acid-functionalized nanoparticles (LA-Al₂O₃) were collected from the suspension by centrifugation (10 min at 3780xg). They were then resuspended and spun down (10 min at 3780xg) twice in hexadecane and twice in hexane. The particles were dried in vacuum at 30°C for 2 hours. To carbonize the linoleic acid layer, 0.750 g dry LA-Al₂O₃ particles were placed in stainless steel Swagelok cell (1.93 cm³ volume) sealed under argon atmosphere. The sealed cell was heated in a tube furnace at 450°C for 2 hours under a 50 standard cubic centimeters per minute (sccm) flow of forming gas (95% N₂: 5% H₂) and then cooled overnight, producing Al₂O₃ nanoparticles with a thin carbon shell. We refer to these nanoparticles as Al₂O₃@C NPs. The gas flow is intended to prevent oxidation of the outer parts of the cell while heating. Formation and carbonization of carbon films using other fatty acids (listed in SI Table S1) used the same ratios of Al₂O₃ NP, solvent, and fatty acid (1.000 g Al₂O₃ NP: 20 mL hexadecane: 0.128 mmol fatty acid).

Functionalization of carbonized Al₂O₃ nanoparticles (Al₂O₃@C) with 4-pentenoic acid was adapted from previous work in our group using benzoyl peroxide (BPO) to initiate grafting of terminal alkenes to H-terminated carbon surfaces.^{28, 35} In that work, we showed that grafting of alkenes to carbon surfaces via this same approach formed well-defined monolayers exhibiting excellent thermal stability; for example, thermogravimetric analysis showed stability to >250°C. Al₂O₃@C NP (200 mg) was weighed into a 20 mL headspace crimp-seal vial. In a glove box under argon, 6 mL benzene was added to a vial containing 0.980 mmol of 4-pentenoic acid and 70 mg of BPO along with 4Å molecular sieves and left to dry for 30 min. Dry solvent, ligand, and BPO were transferred to headspace vial containing Al₂O₃@C NP and the vial was sealed, vortexed to suspend particles, and heated for 3.5 h at 80°C under constant stirring. After the functionalization reaction, particles were washed 2x with 10 mL acetone (breaking down any residual polymer

products) by centrifugation at 3048xg for 10 min, then washed 3x with 15 mL ethanol, centrifuging at 3048xg for 10 min. The particle pellet then was dried in a vacuum oven at 30°C overnight.

Scheme 2. EDC coupling of amineterminated molecules to COOH on

Further functionalization of Al₂O₃@C-COOH was done using EDC coupling, forming an amide linkage on the surface (Scheme 2). The functionalization was adapted from previous literature;³⁶⁻³⁷ as descrbed in the Supporting Information. Details on the synthesis and characterization of of nanoruby and Fe₃O₄ nanoparticles can be found in the Supporting Information (SI), with particle characterization shown Fig. S1 and S2. Ruby, Fe₃O₄, and ZnO nanoparticles were carbonized and functionalized following the same procedure used for Al₂O₃ nanoparticles.

Nanomaterial Characterization

X-ray photoelectron spectroscopy data were taken using a Thermo K-alpha XPS with an Al Kα source (1486.6 eV photon energy) at a 45° take-off angle. XPS samples were prepared by suspending nanoparticles in ethanol and the dropcasting onto a clean boron-doped silicon wafer. Measurements were taken at three points on each sample to check for homogeneity.

XPS data were analyzed in CasaXPS. Quantitative measurement of peak areas was performed using a Shirley background fit to compensate for inelastic scattering³⁸ and mixed Gaussian-Lorentzian line shape GL(30). Peak energies were calibrated to the adventitious carbon C(1s) peak at 284.8 eV.³⁹ Carbon thickness values were calculated using areas under Al(2p) and C(1s) photoemission peaks, using a model that uses the Al(2p) emission as an internal standard and

includes the influence of electron scattering within the substrate and carbon layer.⁴⁰ Detailed procedures are included in the Supporting Information.

Infrared data were obtained using a Bruker Vertex 70 spectrometer at 4 cm⁻¹ resolution from 5000 to 700 cm⁻¹. Spectra of nanoparticles were taken using Diffuse Reflectance Infrared Fourier-Transform Spectroscopy (DRIFTS) using 1% by weight of the analyte in a KBr matrix. Spectra reported here are averages of 500 spectra. Spectra of organic reactants were obtained using Attenuated Total Reflectance (ATR) using a diamond ATR element and averaging 100 spectra.

Measurements of nanoparticles size were performed using Dynamic Light Scattering (DLS), while Zeta potential measurements used laser Doppler electrophoresis; both measurements were performed using a Malvern Zetasizer Nano ZS instrument. Samples were typically prepared using a concentration of 0.1 mg/mL and suspending by ultrasonication (10 sec on, 10 sec off) for 1 hour. Size and zeta potential (ZP) values reported are averages of 5 DLS measurements per sample and 10 ZP measurements per sample.

A limited number of samples were characterized using atomic force microscopy to directly measure the monolayer thickness by a "scratch-off" method in which a sample is first imaged, then subjected to a high loading force over a small region while scanning, and the area is then reimaged. ⁴¹ For surface layers that are weakly bound, this method provides a direct measurement of the thickness of the initial molecular layers.

To evaluate the impact of the coatings on fluorescence properties of nanoruby, we measured fluorescence from nanoruby samples before and after carbonization of linoleic acid. 1 mg/mL of nanoruby (bare or carbon-coated) was suspended via 30 min bath sonication in 1% TWEEN-20 solution to ensure nanoparticles remained suspended throughout the analysis. Using an ISS K2

spectrofluorometer, samples were excited at 410 nm, the maximum peak of the ruby excitation spectrum,⁴² and emission was collected from 670 nm – 710 nm (0.5 nm step size).

Thermogravimetric analysis measurements were done using a TA Q500 thermogravimetric analyzer, measuring mass change for 10-15 mg of sample under N_2 gas flow from 25°C – 800°C.

Raman measurements were taken using a Thermo-Fischer Scientific DXRxi Raman imaging microscope using 532 nm laser excitation and 10x objective. The laser used for planar Al₂O₃ was 2.0 mW, and for Fe₃O₄ NP was 3.0 mW. Scanning electron micrographs were taken on a Leo Supra55 VP SEM at 1-3 kV electron voltage using a secondary electron detector.

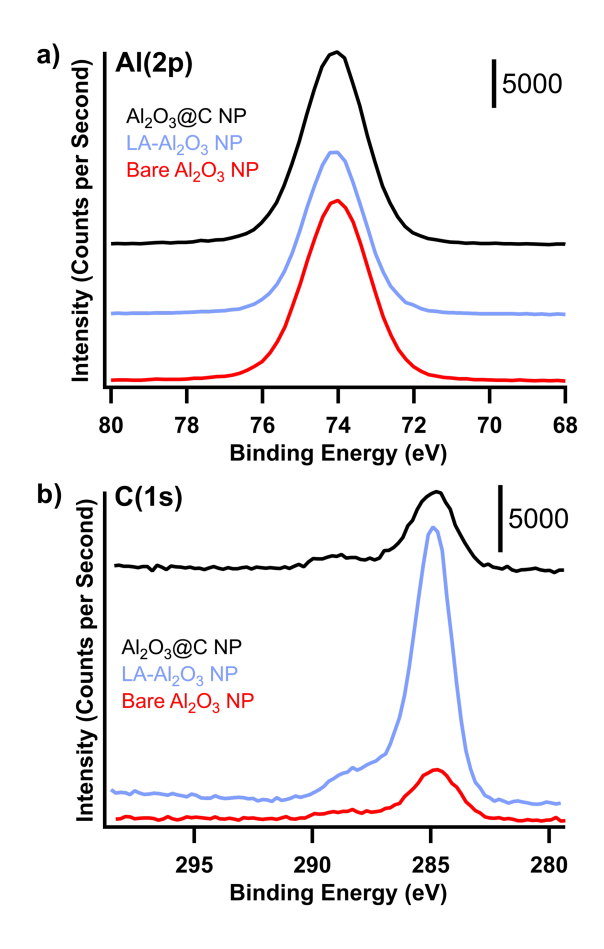


Figure 1. XPS spectra of (a) the Al(2p) region and (b) the (C(1s) region of Al₂O₃ NP untreated, after linoleic acid adsorption, and after carbonization.

Transmission electron microscopy was done on a Tecnai T12 at an accelerating voltage of 120 kV. Iron oxide nanoparticles were suspended in ethanol via bath sonication. An aliquot of the suspension was then dropped onto a Si₃N₄ grid with 8 nm thick windows (Ted Pella) and allowed to dry overnight. Image analysis was conducted using ImageJ open-source software. The size reported is the average of 142 particles.

Powder X-ray diffraction patterns were collected using a Bruker Advance powder diffractometer fitted with a Cu Kα source and a Lynxeye detector. Samples were prepared by suspending nanoparticles in an isopropyl alcohol solution and dropcasting on a zero-diffraction plate.

RESULTS AND DISCUSSION

Formation and characterization of a thin carbon layer

A key aspect of our work is to form very thin carbon layers of controlled thickness. To understand the transformation of the carbon layer on the aluminum oxide surface, we first look at X-ray photoelectron spectroscopy to determine the thickness of the carbon layer of aluminum oxide nanoparticles before and after carbonization. Figure 1 shows the Al(2p) and C(1s) x-ray photoemission regions of bare (non-functionalized) Al₂O₃ NPs, Al₂O₃ NPs after grafting with linoleic acid (LA-Al₂O₃), and LA-Al₂O₃ NPs after heating as described above to form a carbon shell (Al₂O₃@C NP). While the starting surfaces have a small amount of carbon attributed to adsorption of impurities, intentional adsorption of linoleic acid to the surface significantly increases emission from the C(1s) intensity and decreases the Al(2p) emission, as anticipated for a molecular layer with average thickness of ~ 1 nm. Heating in the closed Swagelok vessel decreases the carbon peak once more. We calculated the effective thickness of the carbon layer based on the C(1s) signal and the attenuation of Al(2p) electrons from the substrate by the carbon overlayer as described in SI, yielding the results shown in Table S2 (Supporting Information). To further verify the initial monolayer formation, we performed AFM scratch-off experiments on planar Al₂O₃ samples that were prepared in the same way as Al₂O₃ NP. These data, included as Figure S3 (Supporting Information) show that the carbon layer is very uniform with no evidence

of patchiness. The XPS and AFM data, summarized in SI Table S2, are in good agreement at ~0.8 nm.

While XPS yields information on the type of carbon produced by carbonization, we also used infrared spectroscopy, thermogravimetric analysis, and Raman spectroscopy to further characterize the nature of the carbon-coated surfaces. Figure 2a shows DRIFTS spectra before and after grafting of linoleic acid. The starting Al₂O₃ surface shows a broad feature with superimposed sharp absorption lines in the 3500-4000 cm⁻¹ region from different types of surface -OH groups, with the broad feature arising from strongly hydrogen-bonded groups and the sharp features from different types of isolated (non-hydrogen-bonded) O-H groups. After grafting of linoleic acid, the surface OH groups largely persist, and new peaks are observed at 3000-2800 cm⁻¹ due to C-H stretching vibrations, along with peaks at 1701 cm⁻¹ and 1585 cm⁻¹. The 1701 and 1585 cm⁻¹ peaks are similar to features reported previously, attributed to C=O stretching vibrations of the carboxylic acid head of adsorbed linoleic acid and to the asymmetric stretch of adsorbed carboxylate anions groups, respectively.43. To confirm that the C-H features arose from LA and not from contaminants, we also performed a similar study using partially deuterated linoleic acid (SI, Fig. S4). The spectra of partially deuterated LA show the appearance of new features at 2219 cm⁻¹ and 2200 cm⁻¹, corresponding to the symmetric and asymmetric C-D stretches observed in IR spectrum of neat d₁₁-linoleic acid.⁴⁴ After carbonization, Fig. 2a shows that the C-H features (2800-3000 cm⁻¹ 1) and s C=O feature (1701 cm⁻¹) are absent, but the 1585 cm⁻¹ carboxylate peak persists. These data are consistent with the partial loss of carbon from the surface detected by XPS upon heating. Finally, after heating, the C-H features in the 2800-3000 cm⁻¹ region that are clearly visible in the

LA-Al₂O₃ IR spectrum, are absent in the Al₂O₃@C spectrum. This change indicates that the molecules have largely thermally decomposed, replacing C-H bonds with C-C bonds.

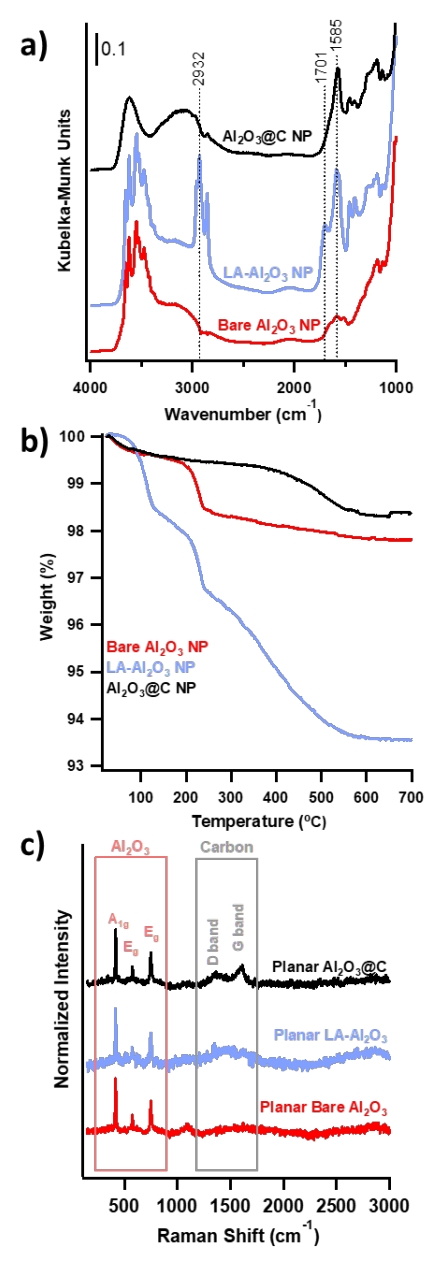


Figure 2. Characterization of bare Al_2O_3 nanoparticles, linoleic acid monolayers adsorbed on Al_2O_3 (LA-Al₂O₃), and Al_2O_3 after forming LA monolayers followed by thermal treatment ($Al_2O_3@C$). (a) diffuse reflectance IR, (b) thermal gravimetric analysis, and (c) Raman spectroscopy (normalized to intensity of the Al_2O_3 A_{1g} phonon line).

Fig. 2b shows thermogravimetric analysis (TGA) on the Al₂O₃ NP, giving additional insight to the thermal stability of the carbon species on the surface. The TGA data in Fig. 2b show that the starting Al₂O₃ nanoparticles exhibit mass loss near 250°C; this has been observed previously and attributed to the desorption of strongly chemisorbed (and possibly dissociated) water from Al₂O₃ surfaces.⁴⁵ After grafting of linoleic acid the nanoparticles exhibit additional losses near 100°C, which we attribute to desorption of loosely bound water. After carbonization, these loss features disappear, and mass loss from the Al₂O₃@C NP begins near 450°C compared to 170°C-210°C reported for near LA in air.46 The absence of the water features near 100°C and 250°C is consistent with the fact that carbon coatings produced from fatty acids under non-oxidizing conditions are expected to be hydrophobic, and therefore are expected to be comparatively immune to acquisition of surface water films. Previous studies have suggested that decomposition at temperatures near 450°C is characteristic of formation of graphitic-like surface layers.⁴⁷ We conducted measurements at different carbonization temperatures, with data shown in Supporting Information (Fig. S5); these data show that by increasing carbonization temperature (250°C, 350°C, or 450°C), the resultant carbon mass on the surface decreases, but the temperature at which the remaining carbon decomposes increases by almost 100°C. We chose to focus further studies on the highest temperature (450°C), due to its high thermal stability while remaining within the thermal limits of the Swagelok cell.

Fig. 2c shows Raman spectra of Al₂O₃(0001) samples at different preparation stages. The data shown here were performed on single-crystal substrates. All three samples show sharp features below 1000 cm⁻¹ due to phonons of bulk alumina. After carbonization, new features appear at 1600±2 cm⁻¹ and a broader feature near 1360 cm⁻¹ that correspond to the widely known "G" and "D" bands of carbon.⁹ Prior studies have shown that the sp² vs. sp³ character of carbon materials

can be characterized by the frequency of the Raman shift of the G band and the ratio of intensities of the D and G bands.⁴⁸ For planar $Al_2O_3@C$, the G band Raman shift of 1600 ± 2 cm⁻¹ indicates high sp² content, while the intensity ratio I(D)/I(G) of 0.60 ± 0.04 suggests ~70% sp² character. This graphitization of carbon indicated by TGA and Raman spectroscopy can also be seen visually after carbonization (SI Fig. S6) as the particles after functionalization have a slight gray appearance.

Control of carbon layer thickness

To determine the extent to which the carbon coating can be controlled through choice of the molecular precursor, we used fatty acids with varying chain length and degree of saturation as the carbon source (identified in SI Table S1) and characterized the effective thickness of the carbon layer with XPS, using methods identical to those outlined above. These experiments show that varying the chain length from 18 to 22 carbon atoms did not have a statistically different impact on carbon thickness (SI Figure S7), although due to the relatively narrow range of lengths investigated a weak length dependence cannot be ruled out. More importantly, varying the degree of saturation has a very strong trend. Figure 3 shows the effective thickness of the carbon layer measured by XPS for 20-carbon-long fatty acids with different degrees of saturation. While the molecules all form adsorbed monolayers with similar density, the molecules with higher degrees of unsaturation yielded layers with greater effective thickness. This increase suggests that

unsaturated C=C bonds are the key sites that lead to thermal cross-linking and the carbon shell formation.

Information from X-ray photoelectron spectroscopy, atomic force microscopy, infrared spectroscopy, thermogravimetric analysis, and Raman spectroscopy, when examined in tandem, indicate the formation of a 1-2 nm monolayer of fatty acid on the surface of alumina upon adsorption. Upon carbonization, this monolayer graphitizes to a carbon shell less than 1 nm thick.

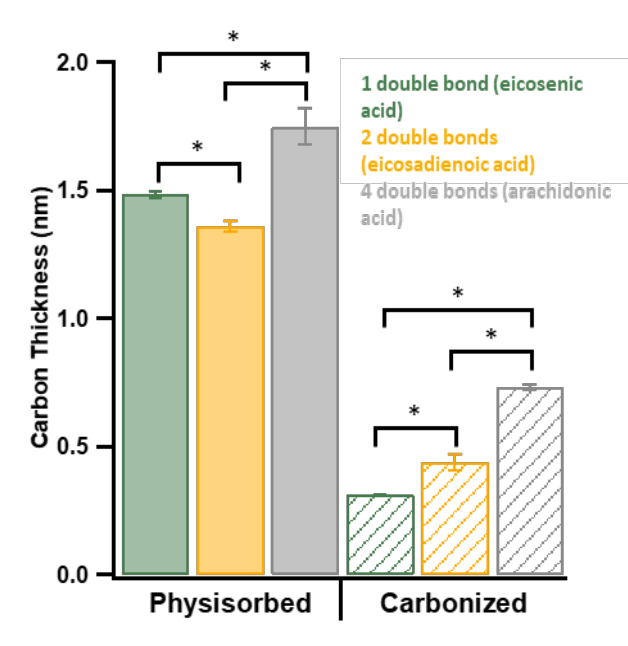


Figure 3. Carbon thickness calculated from XPS for fatty acids with chain lengths of 20 and varying degrees of saturation before and after carbonization. Error bars represent standard error of the mean of 4 measurements. Asterisks indicate statistical significance at the 95% confidence level.

The increase in effective layer thickness with increasing degree of unsaturation implies that unsaturated bonds enhance the cross-linking.

Impact of carbonization on nanoruby optical properties

In the above experiments, we used Al₂O₃ as a model system in part because of the unusual optical properties of Cr³⁺:Al₂O₃ (ruby). In particular, ruby has a very broad absorption spectrum extending throughout much of the visible spectrum region while

emitting in a narrow emission line near 694 nm with quantum efficiency exceeding 80% and a long lifetime of several milliseconds.⁴⁹⁻⁵¹ The long lifetime enables discrimination between nanoruby and other fluorescence emitters based on the vastly different lifetimes, while the broad absorption and narrow emission make it well suited for use with conventional laboratory microscopes, with broadband excitation sources. Furthermore, because the fluorescence emission

from ruby arises from a point defect in the bulk, the emission wavelength and quantum efficiency are only weakly dependent on strain and other effects.⁴² This high degree of optical stability enables ruby in nanoparticle form ("nanoruby") to have highly stable emission properties, in contrast to many other types of luminescent nanoparticles.⁵² All of the above properties make nanoruby well suited to practical utility in a wide range of imaging applications, particularly in biological and/or environmental systems, except for the difficulty of functionalizing Al₂O₃ surfaces in a stable manner using conventional approaches.

We prepared nano-ruby following previously published procedures² ^{34,53-54} as described in the SI and carbonized using the same protocol as used for Al₂O₃ NPs. XPS measurements of nanoruby yielded an effective LA layer thickness of 1.5 nm, and a C thickness of 0.73±0.13 nm after carbonization. These values are similar to those obtained on the planar Al₂O₃(0001) sample described above. We note that nanoruby is synthesized by a process that first forms thin sheets exposing the (0001) face that are then mechanically milled to smaller pieces. Although we have not characterized the detailed distribution of crystal faces from nanoruby, our data suggest that the preferred (0001) face may facilitate adsorption of LA and subsequent carbonization.

We measured the impact of this ~1 nm carbon layer on the emission intensity from nanoruby. Fig. 4 shows the 694 nm emission line from an aqueous suspension of carbon-coated

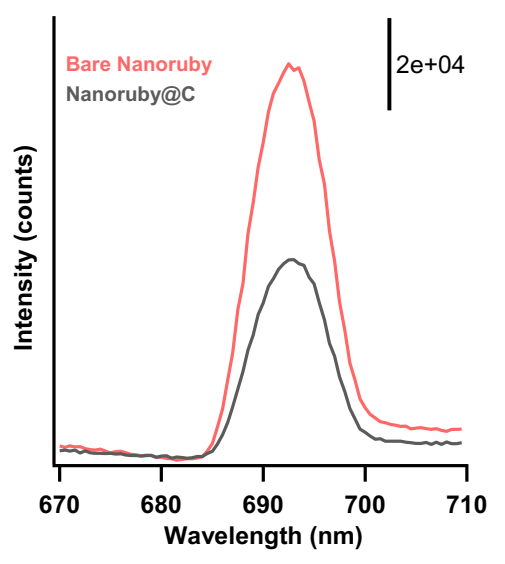


Figure 4. Fluorescence spectra of bare and carbonized nanoruby near the primary ruby emission line.

nanoruby compared with that from an aqueous suspension of non-coated nanoruby at the same mass concentration. The net fluorescence intensity was decreased to 52% of its original value. This reduction in intensity reflects the combined impact of the C layer on both absorption and emission. While there is some reduction in emission intensity, the C layer is sufficiently thin that the carbon-coated nanoruby retains the desired optical properties of the pristine nanoruby and remains a useful optical probe, with the added advantage of being endowed with a carbon coating amenable to further covalent functionalization with C-C surface linkages.

Carbon shell formation on other metal oxides

We broadened the application of the carbon coating process to other metal oxides of interest, using Fe₃O₄ and ZnO as model system. Fe₃O₄ is of potential interest due to its magnetic properties,

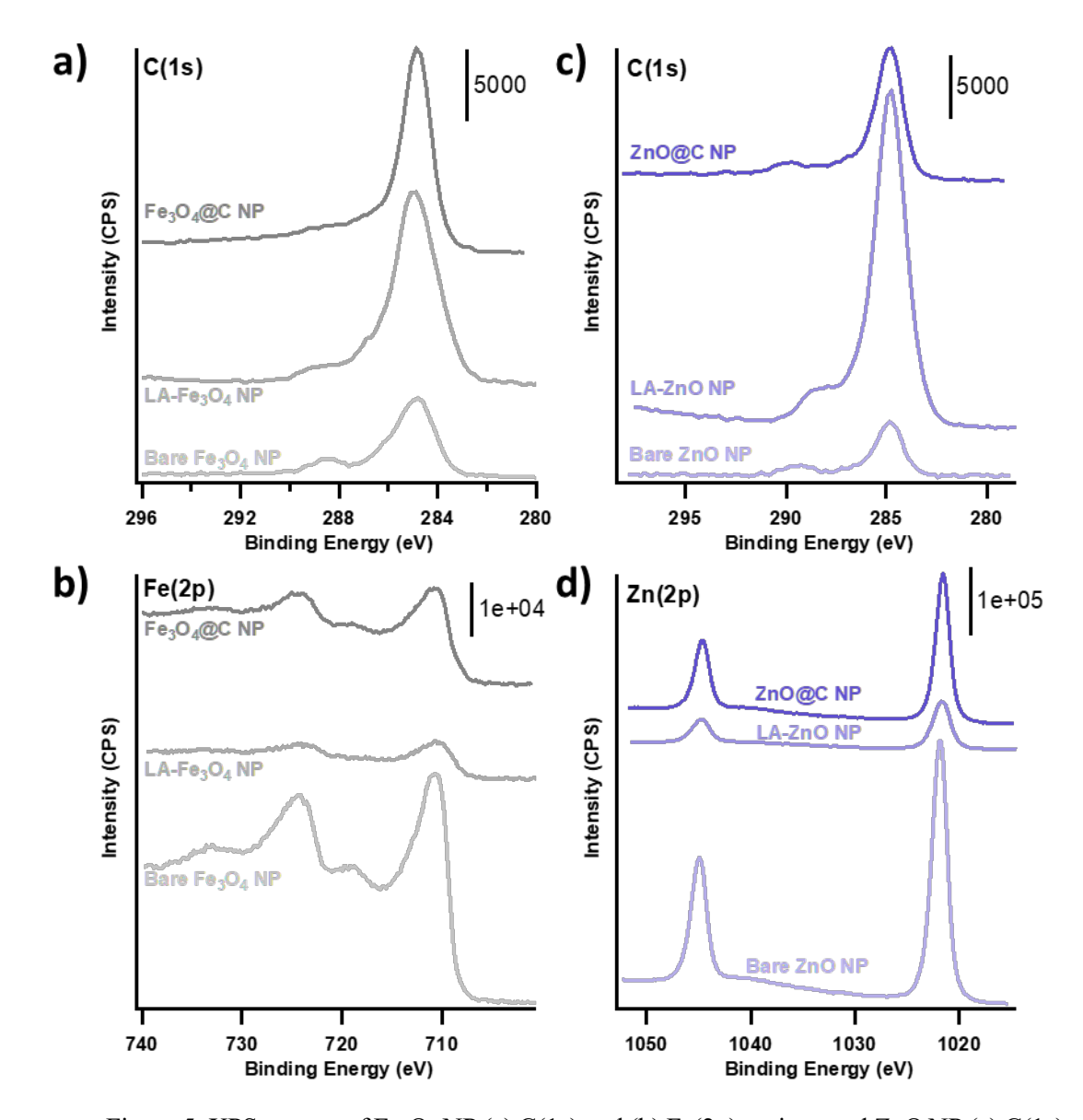


Figure 5. XPS spectra of Fe_3O_4 NP (a) C(1s) and (b) Fe(2p) regions and ZnO NP (c) C(1s) and (d) Zn(2p) regions for bare, LA-adsorbed, and carbonized particles.

shows XPS spectra for the C(1s) region and the metal (2p) region of interest from Fe₃O₄ and ZnO NPs after functionalization with LA and subsequent carbonization. Both Fe₃O₄ NP and ZnO NPs exhibit an increase in the C(1s) intensity and attenuation of Fe(2p) and Zn(2p), respectively, upon the adsorption of linoleic acid to the particle surface. After carbonization, the C(1s) intensity decreases and the metal (2p) intensities are partially restored. These changes follow the same

patterns as Al₂O₃ NP and indicate that during the thermal treatment there is some irreversible desorption of the molecular layer, in addition to decomposition to form the carbon layer. . Table S3 summarizes the effective C layer thickness for each nanoparticle. The carbon coating thickness on Fe₃O₄ and ZnO are similar to those of Al₂O₃ NP, with 1-2 nm of carbon on the surface after linoleic adsorption and a reduction in thickness upon carbonization. These results suggest that the carbon layer formation can be extended to metal oxides of different compositions, but the thickness may vary with the chemical composition of the core nanoparticle. These core-dependent differences likely arise from differences in packing density of the initial monolayers, or due to differences in the extent of thermal desorption from the various metal oxide surfaces.

Raman spectra of Fe₃O₄@C NP (SI, Figure S8) show the appearance of strong D and G bands, similar to those seen on planar Al₂O₃@C (Fig. 2c). The G-band energy (1592 ± 1 cm⁻¹) and I(D)/I(G) intensity ratio (0.71 ± 0.08) are similar to those observed for Al₂O₃@C and again consistent with formation of surface layers with high sp² content. Carbonization and formation of surface graphitic layers also leads to a darkening of the ZnO NPs (which are initially yellow-white in color) and the Al₂O₃ NPs (See SI, Fig. S9). Overall, the XPS and Raman data show that carbonization as described here appears to be a general method that can be applied to form a very thin carbon coating on metal oxides of interest.

Secondary functionalization of thin carbon layer on metal oxide nanoparticles

A strong motivation for using carbon coatings is that, in addition to providing chemically stable coatings, they can also provide a pathway to robust chemical functionalization by grafting of suitable molecules to the carbon coating. $^{28-30, 56}$ To demonstrate this, we investigated functionalization of $Al_2O_3@C$ with molecules bearing different terminal substituent groups that allow control over the charge and hydrophobicity of the functionalized end products. We achieve

this using a approach reported previously using the thermal radical initiator benzoyl peroxide (BPO) to activate the carbon surface, making it reactive toward organic alkenes. The stable, thin carbon surface on the aluminum oxide provides a platform for covalent functionalization using the thermal radical initiator benzoyl peroxide (BPO) and EDC coupling To demonstrate functionalization with a negatively charged terminal group, we used radical-initiated grafting²⁸ to link 4-pentenoic acid to the carbonized surface on Al₂O₃@C NP. To confirm functionalization, we performed controls, running the reaction without benzoyl peroxide and without 4-pentenoic acid. Figure 6a shows C(1s) XPS spectra of Al₂O₃@C NPs before and after grafting of 4-pentenoic acid; also shown are control samples in which either the 4-pentenoic acid ("no acid") or the BPO initiator ("no BPO") was eliminated. While all spectra show some carbon associated with normal level of physically adsorbed contaminants, the spectrum of the sample with both BPO and 4-pentenoic acid present in the reaction mixture clearly shows a stronger C(1s) emission intensity than the others. Quantitative analysis of the C(1s) intensity using the Al(2p) line as an internal standard shows that functionalization with 4-pentenoic acid in the presence of BPO increases the effective carbon thickness from 0.40±0.06 nm for Al₂O₃@C to 1.34±0.01 nm for Al₂O₃@C-COOH. Additionally, the XPS spectrum for the fully grafted sample shows a clear peak at 288.8 eV; this energy is widely regarded as characteristic of carboxylic acid groups.⁵⁷⁻⁵⁹ The presence of this peak is consistent with prior work showing that the functionalization method used here grafts molecules via their terminal olefin group.²⁸ Thus, our data indicate that grafting with 4-pentenoic acid leaves a surface terminated with carboxylic acid groups. Without BPO or 4-pentenoic acid, the C=O peak at 288.8 eV does not grow in, and the carbon thickness does not increase significantly (0.603±0.006 nm for Al₂O₃@C-COOH without the 4-pentenouc acid reactant and 0.595±0.013 nm Al₂O₃@C-COOH without BPO). In a previous study using this same functionalization approach on different carbon

surfaces, we found molecular densities of 1-2 molecules/nm², depending slightly on the molecule selected. Performing a similar quantitative analysis on the functionalized carbon shells used in the present work is more difficult because the thickness of the carbon shell is similar to the inelastic mean free path of the photoelectrons. Nevertheless, we have estimated the molecular density of pentanoic acid grafted onto $Al_2O_3@C$ NPs based on analysis of the high-binding energy XPS peak (from the carboxylic acid groups) and using the Al and ~285 eV C(1s) peak as an internal standard. This analysis indicates a functionalization density of approximately 1 molecules/nm² (10¹⁴ molecules/cm²) for 5-pentenoic acid, consistent with our previous work.

Confirmation of free carboxylate groups is further supported by infrared spectroscopy. Fig. 6b shows DRIFTS spectra of Al₂O₃@C NP at various stages of functionalization, showing a COOH peak at 1706 cm⁻¹, C-H deformation peaks at 1409 cm⁻¹, and C-C twisting vibrations at 1275 cm⁻¹

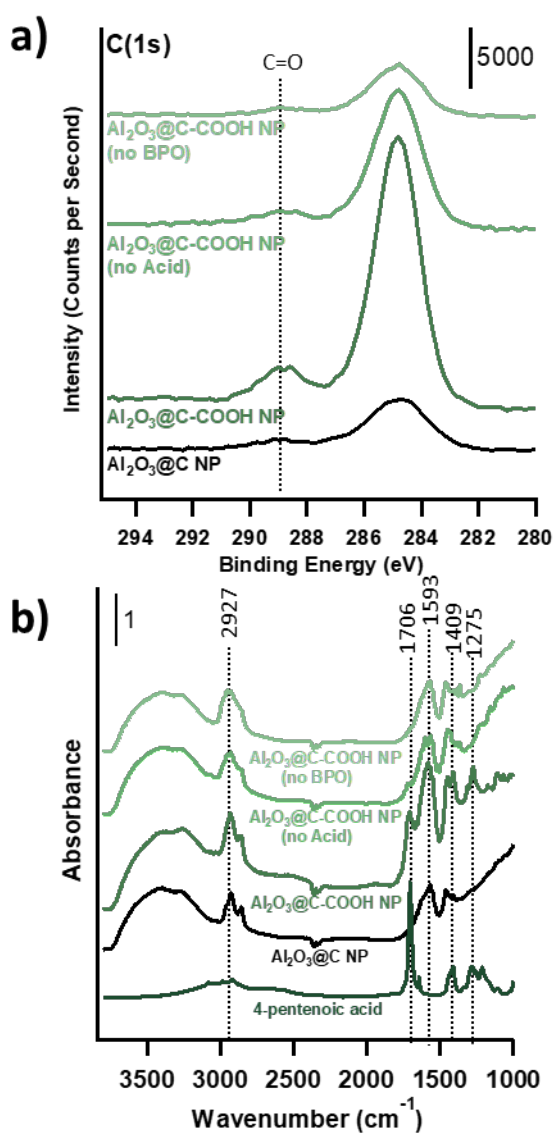


Figure 6. (a) XPS C(1s) region and (b) DRIFTS spectra for Al₂O₃@C NP and carboxylic acid functionalized Al₂O₃@C NP with control samples as indicated.

 $^{1.60}$ These peaks are not present in control samples without BPO ("No BPO") or samples containing BPO but without 4-pentenoic acid ("No acid"). Functionalization with 4-pentenoic acid also changes the zeta potential from $+40.5 \pm 0.4$ mV for Al_2O_3 @C to -28.1 ± 0.2 mV for Al_2O_3 @C-COOH.

While radical-induced grafting can in principle bind molecules with different terminal groups to the surfaces, in practice relatively few molecules with terminal olefin groups are available commercially. Carboxylic acid functional groups like those used above are widely used as building blocks to more complex molecular systems, providing an alternative, versatile way to build on the carbon coating to provide a wider range of functional groups. To demonstrate this capability, we further modified the carboxylic acid-modified

Al₂O₃@C NPs using EDC coupling, as depicted in Scheme 2. EDC coupling links carboxylic acids

to primary amines via an amide linkage, enabling commercially available molecules with various chemical properties to be linked to the Al₂O₃@C NPs.

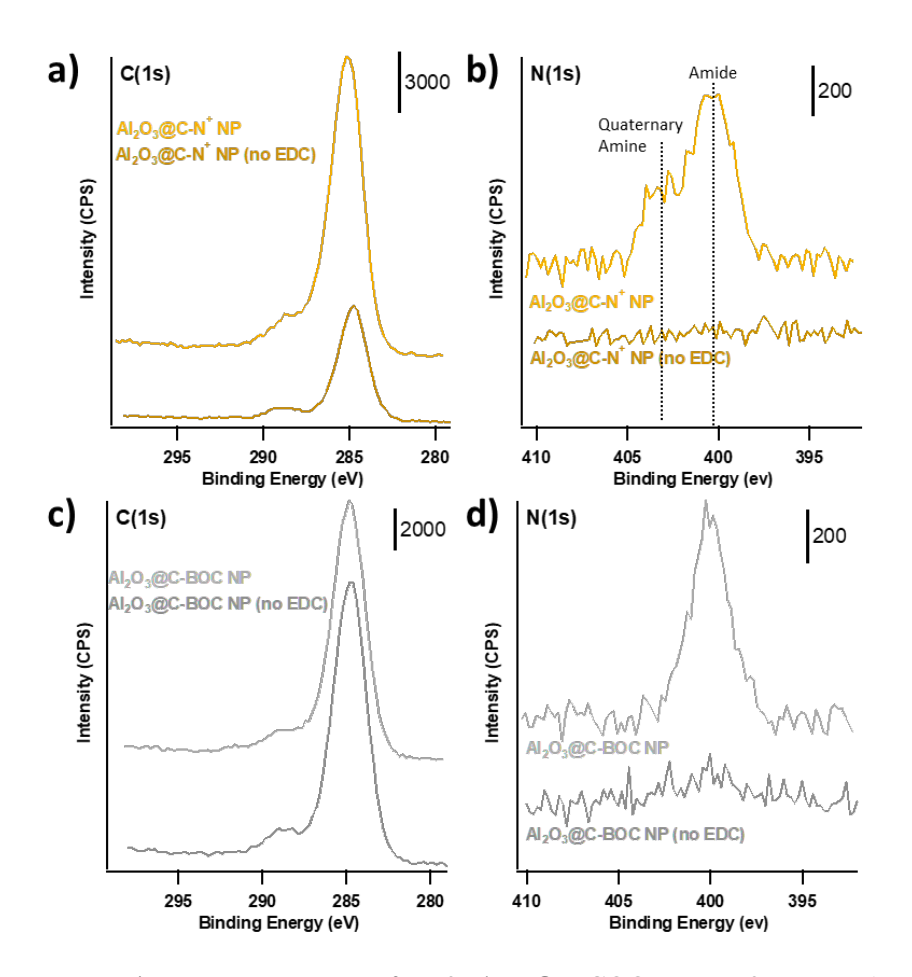


Figure 7. XPS spectra for of Al₂O₃@C-COOH NPs after secondary EDC coupling to provide additional surface functionality. a) and b) show C(1s) and b) N(1s) spectra after linking to a quaternary amine to form Al₂O₃@C-N⁺ NPs. Panels c) and d) show C(1s) and N(1s) spectra after linking to a BOC. All spectra also include "No EDC" control samples in which the EDC coupling agent was intentionally not included. Emission intensities are in counts per second (CPS)

Using EDC chemistry, we linked carboxylic acid-modified Al₂O₃@C NP to three different molecules: (1) N-BOC-ethylenediamine, (2) 1H, 1H-undecafluorohexylamine, and (3) (2-aminoethyl)trimethylammonium chloride hydrochloride, all depicted in Scheme S2 (Supporting Information). We selected these molecules because they provide different surface charges, and

hydrophobic/hydrophilic character, which are primary factors controlling the stability and biological impact of nanoparticles.⁶¹⁻⁶² We label the resulting functionalized Al₂O₃ NP as Al₂O₃@C-BOC, Al₂O₃@C-Fluro, and Al₂O₃@C-N⁺. As with 4-pentenoic acid, we established covalent bond formation using EDC coupling by comparing with control samples in which the EDC coupling agent was intentionally not included.

Fig. 7 shows XPS spectra demonstrating successful linking of BOC-ethylenediamine and 1H, 1H-undecafluorohexylamine to Al₂O₃@C-COOH NPs via EDC coupling. Figure 7 shows that the reaction run with EDC and sulfo-NHS using quaternary amine and BOC ligands, nitrogen peaks appear in the N(1s) XPS region (Fig 7b and 7d), along with an increase in carbon coverage (Fig 7a and 7c). For Al₂O₃@C-N⁺, there are two distinct N(1s) peaks that appear at binding energies typically attributed to amide and quaternary amine N species.⁶³ Control samples containing the aminated ligand but without the EDC coupling agent ("no EDC") show no detectable nitrogen, thereby demonstrating that the N signals from the samples functionalized with EDC are a result of covalent bonding and not nonspecific binding or physisorbed ligands.

Fig. S8 (Supporting Information) shows C(1s), N(1s) and F(1s) spectra demonstrating functionalization with the perfluorinated ligand. These spectra demonstrate increased N(1s) and F(1s) peaks in XPS, along with distinct C=O and C-F peaks in the C(1s) region. Without EDC, there is no nitrogen detected in the N(1s) region, but a small amount of fluorine in F(1s), which is likely from residual fluorine from a small amount of physisorbed ligand. Table S4 summarizes the XPS data from the functionalized surfaces for relevant atomic species.

We further characterized surface functionalization using zeta potential measurements and

dynamic light scattering (DLS) measurements of nanoparticle hydrodynamic diameter, yielding the values shown in SI, Table S5. Fig. 8 summarizes the zeta potentials for the COOH-terminated and bare Al₂O₃ NPs, along with functionalized samples and controls in which the EDC coupling agent was left out. While the bare and C-coated NPs have positive zeta potential, after initial functionalization with carboxylic acid groups the zeta potential is strongly negative. The three controls without EDC have

 $\zeta \sim -15$ mV, indicating the continued presence of

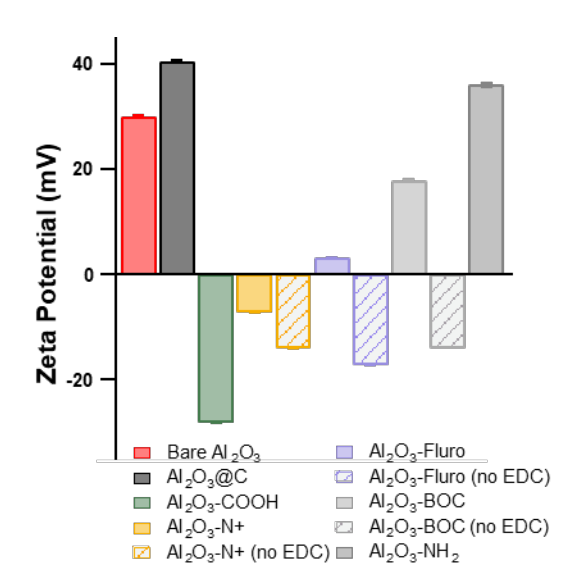


Figure 8. Comparison of zeta potentials for various secondary functionalizations of Al₂O₃@C NP.

exposed carboxylic acid groups. On the functionalized samples with EDC present, $Al_2O_3@C$ -Fluoro NPs have a $\zeta = 3.18 \pm 0.10$ mV, which is expected for a hydrophobic, fluorinated surface species. The NPs modified with a quaternary amino group, $Al_2O_3@C$ -N⁺ yield $\zeta = -7.2 \pm 0.5$ mV. While the quaternary amino group is positively charged, we believe that the resulting intermediate ζ occurs because the density of carboxylic acid groups produced in the initial functionalization is high, and it may not be possible to functionalize all the -COOH groups with the quaternary amine due to steric constraints; the resulting surface is therefore likely a mixture of covalently linked quaternary amino groups and unreacted COOH groups. This interpretation is supported by N(1s) XPS data indicating that density of quaternary amines is lower than that of the starting carboxylic acid groups. In contrast, EDC coupling with the BOC ligand followed by deprotection using

trifluoroacetic in dichloromethane to produce $Al_2O_3@C-NH_2$, has a strongly positive zeta potential of $+36.0 \pm 0.8$ mV.

The carbon coating on Al_2O_3 nanoparticles can be successfully functionalized using thermal-radical initiation and EDC coupling to produce a variety of particles with varying surface charges, ranging from -25 mV to +36 mV, and chemical species, containing carbon, nitrogen, and fluorine groups.

CONCLUSION

The long-term control of chemical surface species on metal oxide nanoparticles is an important aspect when using them in complex biological systems. We have shown that a thin graphitic carbon surface can be applied to a variety of metal oxide nanoparticles through the thermal decomposition of adsorbed fatty acids without significant impact to core properties such as fluorescence. This carbon coating can then be further functionalized with ligands of varying charge and chemical composition via direct C-C surface linkages, providing extraordinary chemical stability in harsh environments like those commonly found in biological studies²⁸⁻³⁰ and opening the door to even further modification using common chemical conjugation methods such as EDC coupling. Ultimately the presence of a thin carbon shell provides a powerful tool for the long-term surface control of metal oxides, offering the ability to further understand the interactions of nanoparticles in biological and biomedical applications.

ASSOCIATED CONTENT

Supporting Information. Procedures for nanoparticle synthesis; additional characterization data. Equations used for analysis of XPS data.

AUTHOR INFORMATION

Corresponding Author

*rjhamers@wisc.edu

Present Addresses.

†Argonne National Laboratory, 9700 S. Cass Ave, Lemont, IL 60430, USA

*Sigma-Aldrich Co., 645 Science Dr, Madison, WI 53711, USA

§Corteva Biosciences, 9330 Zionsville Rd, Indianapolis, IN 46268, USA

Author Contributions

The manuscript was written through contributions of all authors. All authors have given approval to the final version of the manuscript.

Funding Sources

National Science Foundation, CHE-2001611

National Science Foundation, DMR-1720415

ACKNOWLEDGMENT

This work was supported by the National Science Foundation under Grant No. CHE-2001611, the NSF Center for Sustainable Nanotechnology, a part of the NSF Centers for Chemical

Innovation Program. The authors acknowledge use of shared X-ray photoelectron spectrometer, Raman spectrometer, thermal gravimetric analyzer, and transmission electron microscope in the UW Madison Materials Science Center, which is partially supported by NSF through the University of Wisconsin Materials Research Science and Engineering Center (DMR-1720415).

ABBREVIATIONS

XPS, x-ray photoelectron spectroscopy; DRIFTS, Diffuse-reflectance infrared Fourier transform spectroscopy; DLS, Dynamic light-scattering.

REFERENCES

- 1. Albanese, A.; Tang, P. S.; Chan, W. C. W., The effect of nanoparticle size, shape, and surface chemistry on biological systems. *Annual Review of Biomedical Engineering*, **2012**, *14*, 1-16.
- 2. Sreenivasan, V. K. A.; Wan Razali, W. A.; Zhang, K.; Pillai, R. R.; Saini, A.; Denkova, D.; Santiago, M.; Brown, H.; Thompson, J.; Connor, M.; Goldys, E. M.; Zvyagin, A. V., Development of bright and biocompatible nanoruby and its application to background-free timegated imaging of G-protein-coupled receptors. *ACS Applied Materials & Interfaces* **2017**, *9*, 39197-39208.
- 3. Yang, X. H.; Maleki, A.; Lipey, N. A.; Zheng, X. L.; Santiago, M.; Connor, M.; Sreenivasan, V. K. A.; Dawes, J. M.; Lu, Y. Q.; Zvyagin, A. V., Lifetime-engineered ruby nanoparticles (tau-rubies) for multiplexed imaging of mu-opioid receptors. *ACS Sensors* **2021**, *6*, 1375-1383.

- 4. Edmonds, A. M.; Sobhan, M. A.; Sreenivasan, V. K. A.; Grebenik, E. A.; Rabeau, J. R.; Goldys, E. M.; Zvyagin, A. V., Nano-ruby: A promising fluorescent probe for background-free cellular imaging. *Particle and Particle Systems Characterization* **2013**, *30*, 506-513.
- 5. Hoang, K. N. L.; Wheeler, K. E.; Murphy, C. J., Isolation methods influence the protein corona composition on gold-coated iron oxide nanoparticles. *Analytical Chemistry* **2022**, *94*, 4737-4746.
- 6. Casula, M. F.; Floris, P.; Innocenti, C.; Lascialfari, A.; Marinone, M.; Corti, M.; Sperling, R. A.; Parak, W. J.; Sangregorio, C., Magnetic resonance imaging contrast agents based on iron oxide superparamagnetic ferrofluids. *Chemistry of Materials* **2010**, 22, 1739-1748.
- 7. Lowry, G. V.; Gregory, K. B.; Apte, S. C.; Lead, J. R., Transformations of nanomaterials in the environment. *Environmental Science & Technology* **2012**, *46*, 6893-6899.
- 8. Sukhanova, A.; Bozrova, S.; Sokolov, P.; Berestovoy, M.; Karaulov, A.; Nabiev, I., Dependence of nanoparticle toxicity on their physical and chemical properties. *Nanoscale Research Letters* **2018**, *13*, 44.
- 9. Kelkar, S. S.; Reineke, T. M., Theranostics: Combining imaging and therapy. *Bioconjugate Chemistry* **2011**, *22*, 1879-1903.
- 10. Carofiglio, M.; Laurenti, M.; Vighetto, V.; Racca, L.; Barui, S.; Garino, N.; Gerbaldo, R.; Laviano, F.; Cauda, V., Iron-doped ZnO nanoparticles as multifunctional nanoplatforms for theranostics. *Nanomaterials* **2021**, *11*, 2628.
- 11. Ren, X. Q.; Chen, H. W.; Yang, V.; Sun, D. X., Iron oxide nanoparticle-based theranostics for cancer imaging and therapy. *Frontiers of Chemical Science and Engineering* **2014**, *8*, 253-264.

- 12. Servin, A.; Elmer, W.; Mukherjee, A.; De la Torre-Roche, R.; Hamdi, H.; White, J. C.; Bindraban, P.; Dimkpa, C., A review of the use of engineered nanomaterials to suppress plant disease and enhance crop yield. *Journal of Nanoparticle Research* **2015**, *17*, 1-21.
- 13. Ma, C. X.; Borgatta, J.; Hudson, B. G.; Tamijani, A. A.; de la Torre-Roche, R.; Zuverza-Mena, N.; Shen, Y.; Elmer, W.; Xing, B. S.; Mason, S. E.; Hamers, R. J.; White, J. C., Advanced material modulation of nutritional and phytohormone status alleviates damage from soybean sudden death syndrome. *Nature Nanotechnology* **2020**, *15*, 1033-1042.
- 14. Borgatta, J.; Ma, C. X.; Hudson-Smith, N.; Elmer, W.; Perez, C. D. P.; De la Torre-Roche, R.; Zuverza-Mena, N.; Haynes, C. L.; White, J. C.; Hamers, R. J., Copper based nanomaterials suppress root fungal disease in watermelon (*Citrullus lanatus*): Role of particle morphology, composition and dissolution behavior. *ACS Sustainable Chemistry & Engineering* **2018**, *6*, 14847-14856.
- 15. Schubert, U., En route from metal alkoxides to metal oxides: Metal oxo/alkoxo clusters. *Journal of Sol-Gel Science and Technology*, **2023** *105*, 587–595.
- 16. Schubert, U., Surface chemistry of carboxylato-substituted metal oxo clusters model systems for nanoparticles. *Coordination Chemistry Reviews* **2017**, *350*, 61-67.
- 17. Deblock, L.; Goossens, E.; Pokratath, R.; De Buysser, K.; De Roo, J., Mapping out the aqueous surface chemistry of metal oxide nanocrystals: Carboxylate, phosphonate, and catecholate ligands. *JACS Au* **2022**, *2*, 711-722.
- 18. Avena, M., The reactivity of the metal oxide-water and mineral-water interfaces an inorganic/coordination viewpoint. *Eur. J. Inorg. Chem.* **2022**, 2022, 10.

- 19. Wang, R. S.; Jakhar, K.; Ahmed, S.; Antao, D. S., Elucidating the mechanism of condensation-mediated degradation of organofunctional silane self-assembled monolayer coatings. *ACS Applied Materials & Interfaces* **2021**, *13*, 34923-34934.
- 20. Zhizhchenko, A. Y.; Shabalina, A. V.; Aljulaih, A. A.; Gurbatov, S. O.; Kuchmizhak, A. A.; Iwamori, S.; Kulinich, S. A., Stability of octadecyltrimethoxysilane-based coatings on aluminum alloy surface. *Materials* **2022**, *15*, 1804.
- 21. Pujari, S. P.; Scheres, L.; Marcelis, A. T. M.; Zuilhof, H., Covalent surface modification of oxide surfaces. *Angewandte Chemie-International Edition* **2014**, *53*, 6322-6356.
- 22. Ostapenko, A.; Kloffel, T.; Eussner, J.; Harms, K.; Dehnen, S.; Meyer, B.; Witte, G., Etching of crystalline zno surfaces upon phosphonic acid adsorption: Guidelines for the realization of well-engineered functional self-assembled monolayers. *ACS Applied Materials & Interfaces* **2016**, *8*, 13472-13483.
- 23. Gouzman, I.; Dubey, M.; Carolus, M. D.; Schwartz, J.; Bernasek, S. L., Monolayer vs. Multilayer self-assembled alkylphosphonate films: X-ray photoelectron spectroscopy studies. *Surface Science* **2006**, *600*, 773-781.
- 24. Parikh, A. N.; Allara, D. L.; Azouz, I. B.; Rondelez, F., An intrinsic relationship between molecular-structure in self-assembled n-alkylsiloxane monolayers and deposition temperature. *Journal of Physical Chemistry* **1994**, *98*, 7577-7590.
- 25. Hoque, E.; DeRose, J. A.; Bhushan, B.; Mathieu, H. J., Self-assembled monolayers on aluminum and copper oxide surfaces: Surface and interface characteristics, nanotribological properties, and chemical stability. In *Applied Scanning Probe Methods IX: Characterization*, Bhushan, B.; Fuchs, H.; Tomitori, M., Eds. Springer-Verlag Berlin: Berlin, 2008; pp 235-281.

- 26. Anderson, A.; Ashurst, W. R., Investigation of the ability of a silica "seed" layer to improve the thermal and aqueous immersion stability of alkylsilane monolayers on silicon oxide surfaces. *Thin Solid Films* **2008**, *516*, 7538-7546.
- 27. Thissen, P.; Valtiner, M.; Grundmeier, G., Stability of phosphonic acid self-assembled monolayers on amorphous and single-crystalline aluminum oxide surfaces in aqueous solution. *Langmuir* **2010**, *26*, 156-164.
- 28. Zhang, Y.; Tamijana, A. A.; Taylor, M. E.; Zhi, B.; Haynes, C. L.; Mason, S. E.; Hamers, R. J., Molecular surface functionalization of carbon materials via radical- induced grafting of terminal alkenes. *Journal of the American Chemical Society* **2019**, *141*, 8277-8288.
- 29. Yang, W. S.; Auciello, O.; Butler, J. E.; Cai, W.; Carlisle, J. A.; Gerbi, J.; Gruen, D. M.; Knickerbocker, T.; Lasseter, T. L.; Russell, J. N.; Smith, L. M.; Hamers, R. J., DNA-modified nanocrystalline diamond thin-films as stable, biologically active substrates. *Nat. Mater.* **2002,** *1*, 253-257.
- 30. Stavis, C.; Clare, T. L.; Butler, J. E.; Radadia, A. D.; Carr, R.; Zeng, H. J.; King, W. P.; Carlisle, J. A.; Aksimentiev, A.; Bashir, R.; Hamers, R. J., Surface functionalization of thin-film diamond for highly stable and selective biological interfaces. *Proc. Natl. Acad. Sci. U. S. A.* **2011**, *108*, 983-988.
- 31. Sun, B.; Colavita, P. E.; Kim, H.; Lockett, M.; Marcus, M. S.; Smith, L. M.; Hamers, R. J., Covalent photochemical functionalization of amorphous carbon thin films for integrated real-time biosensing. *Langmuir* **2006**, 22, 9598-9605.
- 32. Allara, D. L.; Nuzzo, R. G., Spontaneously organized molecular assemblies. 1. Formation, dynamics, and physical properties of n-alkanoic acids adsorbed from solution on an oxidized aluminum surface. *Langmuir* **1985**, *1*, 45-52.

- 33. Kang, Y. S.; Risbud, S.; Rabolt, J. F.; Stroeve, P., Synthesis and characterization of nanometer-size Fe₃O₄ and γ-Fe₂O₃ particles. *Chemistry of Materials* **1996**, 8, 2209-2211.
- 34. Rani, G.; Sahare, P. D., Structural and photoluminescent properties of Al₂O₃:Cr³⁺ nanoparticles via solution combustion synthesis method. *Advanced Powder Technology* **2014**, 25, 767-772.
- 35. Zhang, Y. Q.; Hudson-Smith, N. V.; Frand, S. D.; Cahill, M. S.; Davis, L. S.; Feng, Z. V.; Haynes, C. L.; Hamers, R. J., Influence of the spatial distribution of cationic functional groups at nanoparticle surfaces on bacterial viability and membrane interactions. *Journal of the American Chemical Society* **2020**, *142*, 10814-10823.
- 36. Bachman, B. F.; Jones, Z. R.; Jaffe, G. R.; Salman, J.; Wambold, R.; Yu, Z.; Choy, J. T.; Kolkowitz, S. J.; Eriksson, M. A.; Kats, M. A.; Hamers, R. J., High-density covalent grafting of spin-active molecular moieties to diamond surfaces. *Langmuir* **2021**, *37*, 9222-9231.
- 37. Sehgal, D.; Vijay, I. K., A method for the high efficiency of water-soluble carbodiimide-mediated amidation. *Analytical Biochemistry* **1994**, *218*, 87-91.
- 38. Shirley, D. A., High-resolution x-ray photoemission spectrum of the valence bands of gold. *Physical Review B* **1972**, *5*, 4709-4714.
- 39. Barr, T. L.; Seal, S., Nature of the use of adventitious carbon as a binding energy standard. *Journal of Vacuum Science & Technology A: Vacuum, Surfaces, and Films* **1995**, *13*, 1239-1246.
- 40. Franking, R. A.; Landis, E. C.; Hamers, R. J., Highly stable molecular layers on nanocrystalline anatase TiO₂ through photochemical grafting. *Langmuir* **2009**, 25, 10676-10684.
- 41. Dvir, H.; Jopp, J.; Gottlieb, M., Estimation of polymer-surface interfacial interaction strength by a contact afm technique. *Journal of Colloid and Interface Science* **2006**, *304*, 58-66.

- 42. Seat, H. C.; Sharp, J. H., Dedicated temperature sensing with c-axis oriented single-crystal ruby (Cr³⁺:Al₂O₃) fibers: Temperature and strain dependences of R-line fluorescence. *IEEE Transactions on Instrumentation and Measurement* **2004**, *53*, 140-154.
- 43. Cross, S. N. W.; Rochester, C. H., Infrared study of adsorption of linoleic-acid on alumina immersed in carbon-tetrachloride. *Journal of the Chemical Society-Faraday Transactions I* 1978, 74, 2141-2145.
- 44. Nolin, B.; Jones, R. N., The infrared absorption spectra of deuterated esters: II. Ethyl acetate. *Canadian Journal of Chemistry* **1956,** *34*, 1392-1404.
- 45. López-Juárez, R.; Razo-Perez, N.; Pérez-Juache, T.; Hernandez-Cristobal, O.; Reyes-López, S. Y., Synthesis of α-Al₂O₃ from aluminum cans by wet-chemical methods. *Results in Physics* **2018**, *11*, 1075-1079.
- 46. Li, J.; Liu, J.; Sun, X.; Liu, Y., The mathematical prediction model for the oxidative stability of vegetable oils by the main fatty acids composition and thermogravimetric analysis. *LWT-Food Science and Technology* **2018**, *96*, 51-57.
- 47. Lewis, I., Chemistry of pitch carbonization. Fuel **1987**, 66, 1527-1531.
- 48. Ferrari, A. C.; Robertson, J., Raman spectroscopy of amorphous, nanostructured, diamond–like carbon, and nanodiamond. *Philosophical Transactions of the Royal Society of London. Series A: Mathematical, Physical and Engineering Sciences* **2004**, *362*, 2477-2512.
- 49. Maiman, T. H., Stimulated optical radiation in ruby. *Nature* **1960**, *187*, 493-494.
- 50. Quimby, R. S.; Yen, W. M., Photoacoustic measurement of the ruby quantum efficiency. *Journal of Applied Physics* **1980**, *51*, 1780-1782.
- 51. Zhang, Z.; Grattan, K. T. V.; Palmer, A. W., Temperature dependences of fluorescence lifetimes in Cr³⁺-doped insulating crystals. *Physical Review B* **1993**, *48*, 7772-7778.

- 52. Orfield, N. J.; Majumder, S.; Hu, Z. J.; Koh, F. Y. C.; Htoon, H.; Hollingsworth, J. A., Kinetics and thermodynamics of killing a quantum dot. *ACS Applied Materials & Interfaces* **2020**, *12*, 30695-30701.
- 53. Fatehah, M. O.; Aziz, H. A.; Stoll, S., Stability of ZnO nanoparticles in solution. Influence of pH, dissolution, aggregation and disaggregation effects. *Journal of Colloid Science and Biotechnology* **2014**, *3*, 75-84.
- 54. Razali, W. A. W.; Sreenivasan, V. K. A.; Goldys, E. M.; Zvyagin, A. V., Large-scale production and characterization of biocompatible colloidal nanoalumina. *Langmuir* **2014**, *30*, 15091-15101.
- 55. Gupta, A. K.; Gupta, M., Synthesis and surface engineering of iron oxide nanoparticles for biomedical applications. *Biomaterials* **2005**, *26*, 3995-4021.
- 56. Strother, T.; Knickerbocker, T.; Russell, J. N.; Butler, J. E.; Smith, L. M.; Hamers, R. J., Photochemical functionalization of diamond films. *Langmuir* **2002**, *18*, 968-971.
- 57. Gengenbach, T. R.; Major, G. H.; Linford, M. R.; Easton, C. D., Practical guides for x-ray photoelectron spectroscopy (XPS): Interpreting the carbon 1s spectrum. *J. Vac. Sci. Technol. A* **2021**, *39*, 24.
- 58. Pletincx, S.; Trotochaud, L.; Fockaert, L. L.; Mol, J. M. C.; Head, A. R.; Karslioglu, O.; Bluhm, H.; Terryn, H.; Hauffman, T., *In situ* characterization of the initial effect of water on molecular interactions at the interface of organic/inorganic hybrid systems. *Sci Rep* **2017**, *7*, 8.
- 59. Singh, B.; Fang, Y. Y.; Cowie, B. C. C.; Thomsen, L., Nexafs and XPS characterisation of carbon functional groups of fresh and aged biochars. *Organic Geochemistry* **2014,** 77, 1-10.
- 60. Socrates, G., *Infrared and Raman characteristic group frequencies: Tables and charts*. 3rd ed.; Wiley: 2004.

- 61. Feng, Z. V.; Gunsolus, I. L.; Qiu, T. A.; Hurley, K. R.; Nyberg, L. H.; Frew, H.; Johnson, K. P.; Vartanian, A. M.; Jacob, L. M.; Lohse, S. E., Impacts of gold nanoparticle charge and ligand type on surface binding and toxicity to Gram-negative and Gram-positive bacteria. *Chemical science* **2015**, *6*, 5186-5196.
- 62. Lochbaum, C. A.; Chew, A. K.; Zhang, X.; Rotello, V.; Van Lehn, R. C.; Pedersen, J. A., Lipophilicity of cationic ligands promotes irreversible adsorption of nanoparticles to lipid bilayers. *ACS Nano* **2021**, *15*, 6562-6572.
- 63. Chastain, J.; King Jr, R. C., Handbook of x-ray photoelectron spectroscopy. *Perkin-Elmer Corporation* **1992**, Perkin-Elmer Corp, Eden Prairie, MN ISBN 9780964812413.